

Experimental and Numerical Study of Droplets Hydrodynamics in Microchannels

Flavie Sarrazin, Karine Loubière, Laurent Prat, and Christophe Gourdon
Laboratoire de Génie Chimique de Toulouse (LGC), UMR CNRS/INPT/UPS 5503,
31106 Toulouse, France

Thomas Bonometti and Jacques Magnaudet
Institut de Mécanique des Fluides de Toulouse (IMFT), UMR CNRS/INPT/UPS 5502,
31400 Toulouse, France

This article reports on numerical simulations and experimental determination of the hydrodynamics of liquid–liquid flow in rectangular microchannels. The numerical method is an interface-capturing technique without any interface reconstruction. Micro-particle image velocimetry (micro-PIV) measurements are used to obtain experimental velocity fields inside droplets that are compared to simulations. Finally, injecting a passive tracer in the simulated droplets also helps to obtain a better understanding of the mixing phenomenon. These results allow interpreting mixing defaults during bleaching experiments inside microdroplets. Furthermore, this study leads to important results about interface deformation and velocity fields inside the droplets and in the continuous phase for mass- and heat-transfer studies.

Keywords: hydrodynamics, mixing, micro-droplets, rectangular microchannel, micro-PIV, direct simulation, interface capturing

Introduction

In the pharmaceutical and fine chemicals industries, process fast design is a determining step for economical viability. To reduce this “time to market” constraint, the product development phase can be reduced by improving the initial step concerned with physical and chemical data acquisition. This can be focused on determining chemical kinetics and mass-transfer parameters. A very promising application of two-phase flow in microchannels is to use microdroplets as individual nanovolume batch reactors. Song et al.¹ presented a microfluidic system that may be used to control networks of chemical reactions at the millisecond scale. The reagents are mixed in droplets that flow along a serpentine microchannel. Performing reac-

tions inside the droplets offer many advantages: the products are isolated, transported, and efficiently mixed thanks to convective and diffusive effects inside the droplet. Moreover, the necessary amounts of product are very small and well controlled, which is particularly interesting when the products are toxic or expensive. When the droplet velocity is known, the reaction time inside the droplet grows linearly with the channel length, making chemical kinetics measurements easier. For a better analysis of the experimental data, it is necessary to understand and quantify the phenomena that interact with the reaction, such as droplet formation, transport, and homogenization. At small scales, the capillary and viscous effects dominate and the flow is laminar. The product mixing is then slower than that in a turbulent stream.

In a recent study we performed mixing between dye and water inside the droplets² and showed that the homogenization can be achieved within <10 ms after the product meeting (see Figure 1a). Furthermore, an acid–base instantaneous reaction

Correspondence concerning this article should be addressed to F. Sarrazin at Flavie.Sarrazin@ensiacet.fr.

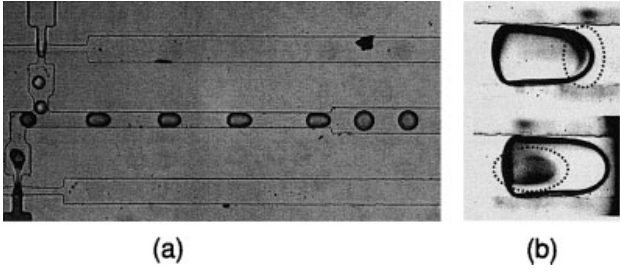


Figure 1. Mixing inside a microchannel where microdroplets are transported in a continuous oil stream (high-frequency image acquisition).

(a) General view of the device. The central channel section is $50 \times 60 \mu\text{m}$. (b) “Dead zones” inside the droplets underlined by a colored acid–base reaction.

followed by a color indicator underlined the presence of dead zones at the front and back of the droplets, where the mixing remains mainly as the result of molecular diffusion, as shown in Figure 1b.³ Understanding this phenomenon is of great importance to analyze the evolution of the concentration inside the droplets and then be able to obtain correct kinetics.

Several studies focused on simulating two-phase flows inside milli- and microchannels. Holdych et al.⁴ studied the stability of a gas–liquid annular stream using a Lattice–Boltzmann method in a two-dimensional (2D) microchannel. Ghidersa et al.⁵ carried out three-dimensional (3D) computations of the hydrodynamics of a bubble chain in a millimetric channel using a Volume of Fluid Method. Harries et al.⁶ used a computational fluid dynamics (CFD) code to investigate the internal flow patterns of segmented flows in a microreactor and the transfer of dissolved species within the segments and across the interfaces. Their simulation was 2D and the segment was assumed to have a rectangular shape. Kashid et al.⁷ studied the internal circulation within liquid slugs in a liquid–liquid microreactor, mainly by focusing on the effect of flow on the circulation time and stagnant region. They performed 2D computations using a CFD particle-tracing algorithm and particle image velocimetry (PIV) was used to visualize the internal circulation within the slugs. Coulliette and Pozrikidis⁸ used a Boundary Element Method to study drop deformation and motion in a circular channel; they considered the particular case where the continuous and dispersed phases have the same viscosity. Muradoglu and Stone⁹ used a Front-Tracking Method to simulate advective effects inside a 2D droplet circulating in a serpentine channel. The droplet shape was calculated self-consistently, molecular mixing was ignored, and only mixing by chaotic advection was considered. This article answers questions regarding the initial mixing of droplets in bending channels and the effect of dimensionless parameters such as the Capillary number (Ca), the Reynolds number (Re), the relative droplet radius, or the viscosity ratio. The authors visualized and measured mixing by using particle tracing.

In the present study, the system is characterized by a strong viscosity contrast between the continuous and dispersed phases within a liquid–liquid system. Besides, the drop shape must be part of the solution and 3D aspects must be taken into account because the channel section is rectangular. It seems that none

of the available numerical studies combines these constraints. We focus on the determination of velocity fields inside droplet strings moving in straight channels. This information should be integrated in studies concerning reaction inside the droplets¹⁰ or transfer phenomena between the two phases.^{11,12} We use a finite-volume/front-capturing method that allows us to perform 2D and 3D simulations at a reasonable cost. Interface deformation and velocity fields inside both the droplets and the continuous phase can be followed. Both the interface and the passive tracer are defined by color functions that are transported by the flow. Therefore no complex or expensive interface tracking is needed. The velocity field inside the droplets obtained by direct numerical simulations is compared to microparticle image velocimetry (micro-PIV) measurements. Furthermore, injecting a passive tracer in the simulated droplets reveals the existence of internal recirculation zones and helps in attaining a better understanding of the mixing phenomenon.

After characterizing the physical situation under consideration, the article describes how we (1) numerically simulate the droplet hydrodynamic, (2) experimentally validate the previous results through PIV measurements, and (3) use these results to explain mixing defaults during bleaching experiments with very fast kinetics.

The Studied Case

Operating conditions

The configuration adopted in this study (both experimentally and numerically) is the following. The microchannel section is rectangular, with a constant width D equal to $60 \mu\text{m}$ and a constant height H equal to $0.83D$. It is filled with silicone oil of density $\rho_c = 950 \text{ kg/m}^3$ and viscosity $\mu_c = 0.02 \text{ kg/(ms)}$. Furthermore, we inject water droplets of density $\rho_d = 1000 \text{ kg/m}^3$, viscosity $\mu_d = 0.001 \text{ kg/(ms)}$, and volume $\mathcal{V}_d = 3 \times 10^{-15} \text{ m}^3$. The surface tension σ between the two liquids is set to $\sigma = 0.01 \text{ N/m}$. These lead to density and viscosity ratios of $\rho_c/\rho_d = 0.95$ and $\mu_c/\mu_d = 20$, respectively. Experimental measurements of the velocity U and the flow rate Q of the continuous and dispersed phases give $U_c = 0.037 \text{ m/s}$ and $Q_c = 11 \times 10^{-11} \text{ m}^3/\text{s}$ for silicone oil and $U_d = 0.070 \pm 0.025 \text{ m/s}$ and $Q_d = 2.8 \times 10^{-11} \text{ m}^3/\text{s}$ for water droplets. The corresponding droplets are about $150 \times 50 \times 40 \mu\text{m}$ (length \times width \times height).

Dimensional analysis

To understand the driving effects in such flows, some characteristic parameters are evaluated: the capillary number Ca, the Weber number We, and the Bond number Bo. They compare capillary effects to viscous, inertial, and gravitational effects, respectively. Considering an equivalent diameter $D_{eq} = 1.33D$, a droplet velocity $U_d = 0.05 \text{ m/s}$, and taking into account the physical properties of the continuous phase previously mentioned, we obtain $\text{Ca} = \mu_c U_d / \sigma = 0.1$, $\text{We} = \rho_c U_d^2 D_{eq} / \sigma = 2 \times 10^{-2}$, $\text{Bo} = |\rho_c - \rho_d| g D_{eq}^2 / \sigma = 3 \times 10^{-4}$ (g denotes gravity), and $\text{Re}_d = \rho_c U_d D_{eq} / \mu_c = 0.19$. Thus the leading effects are in decreasing order: surface tension, viscosity, inertia, and gravity, respectively. The intensity of two successive contributions differs by approximately one order of magnitude. We can also define a viscous time $\tau = \rho_c D_{eq}^2 / \mu_1 \approx 3 \times 10^{-4} \text{ s}$ and a capillary time $\tau_\sigma = (\rho_c D_{eq}^3 / \sigma)^{1/2} \approx 0.73\tau$. We

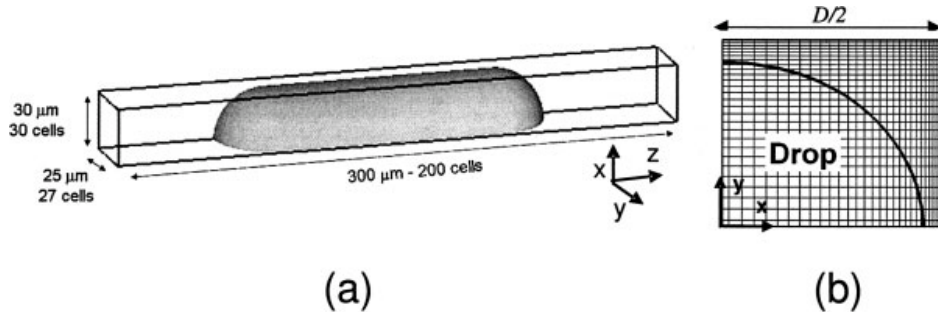


Figure 2. (a) 3D computational domain and initial drop shape; (b) detail of the grid over one quarter of the channel.

The thick line indicates the initial position of the interface.

will see later how the prevalence of capillary affects the numerical time step.

Direct Numerical Simulations

Numerical method

The numerical method is an interface-capturing technique that does not make use of any interface reconstruction. We assume the two fluids to be Newtonian and incompressible, with uniform surface tension. The evolution of the two-phase flow is then classically described using the one-fluid formulation of the Navier–Stokes equations:

$$\frac{\partial U}{\partial t} + U \cdot \nabla U = -\frac{1}{\rho} \nabla P + g + \frac{1}{\rho} \nabla \cdot [\mu(\nabla U + \cdot \nabla U)] - \frac{\sigma}{\rho} (\nabla \cdot n) n \delta_I \quad \nabla \cdot U = 0 \quad (1)$$

where U , P , ρ , and μ are the local velocity, pressure, density, and dynamical viscosity in the flow, respectively; g denotes gravity; and σ is the surface tension. The surface delta function δ_I is zero outside the interface, the unit normal of which (directed toward the continuous phase) is denoted by n . The local volume fraction of water obeys

$$\frac{\partial C}{\partial t} + U \cdot \nabla C = 0 \quad (2)$$

This volume fraction equals one (resp. zero) in cells filled with water (resp. silicone oil) and takes intermediate values in cells belonging to the transition region. The local density and dynamical viscosity are evaluated using a linear interpolation, that is,

$$\rho = C\rho_d + (1 - C)\rho_c \quad \mu = C\mu_d + (1 - C)\mu_c \quad (3)$$

The capillary force is transformed into a volume force using the continuum surface force model proposed by Brackbill et al.¹³ Thus we write

$$\frac{\sigma}{\rho} (\nabla \cdot n) n \delta_I = \frac{\sigma}{\rho} \nabla \cdot \left(\frac{\nabla C}{\|\nabla C\|} \right) \nabla C \quad (4)$$

The Navier–Stokes system of equations (Eq. 1) is solved using the JADIM code developed at Institut de Mécanique des Fluides de Toulouse (IMFT). Details on the spatial discretization and time-advancement algorithm used in this code for con-

stant-density situations may be found in several previous publications.^{14–16} Briefly, the momentum equations are discretized on a staggered orthogonal grid using a finite-volume approach. The spatial discretization is performed using second-order centered differences. Time advancement is achieved through a third-order Runge–Kutta method for advective and source terms and a Crank–Nicolson method for viscous stresses. Incompressibility is satisfied at the end of each time step through a projection method. The overall algorithm is second-order accurate in both time and space.

To solve Eq. 2, we split it into successive one-dimensional steps along each grid direction i ($i = 1, 3$) and use a flux-corrected transport scheme¹⁷ for each substep. To prevent the transition region $0 < C < 1$ from thickening as time proceeds we make the velocity field involved in Eq. 2 locally constant across it. This procedure allows us to keep the thickness of the transition region within three cells all along the computation. Further details about the transport of the volume fraction may be found in Bonometti and Magnaudet.^{18,19}

Computational setup

The computational domain and the grid size are shown in Figure 2. Given that gravity has no significant effect on the flow, we assume the latter to be symmetric along the vertical and horizontal middle planes (xz) and (yz). Only a quarter of the droplet is considered in the 3D simulation. In addition, the configuration of the droplet chain is reduced to the study of a single droplet by applying periodic conditions at the boundaries normal to the mean flow direction (z -axis). Thus the length of the domain defines the frequency of droplet injection. Free-slip conditions are imposed on boundaries corresponding to the droplet symmetry planes; the other boundaries parallel to the mean flow direction are considered as rigid walls. The grid is refined near the walls to capture accurately the liquid film separating the droplets from the walls (see Figure 2b). There are approximately 10 computational cells in the initial liquid film and the size of the smallest cell is $5 \times 10^{-3}D$. The grid size is regular along the mean flow direction with a cell size of $2.5 \times 10^{-2}D$. The dimensions of the initial droplet are $0.73D$, $0.9D$, and $2.93D$ along the x -, y -, and z -directions, respectively. They are such that the droplet volume \mathfrak{V}_d matches that used in the experiments (see The Studied Case section above).

The experimental control parameters are the flow rates of the two liquids. In the computations, droplets are already pres-

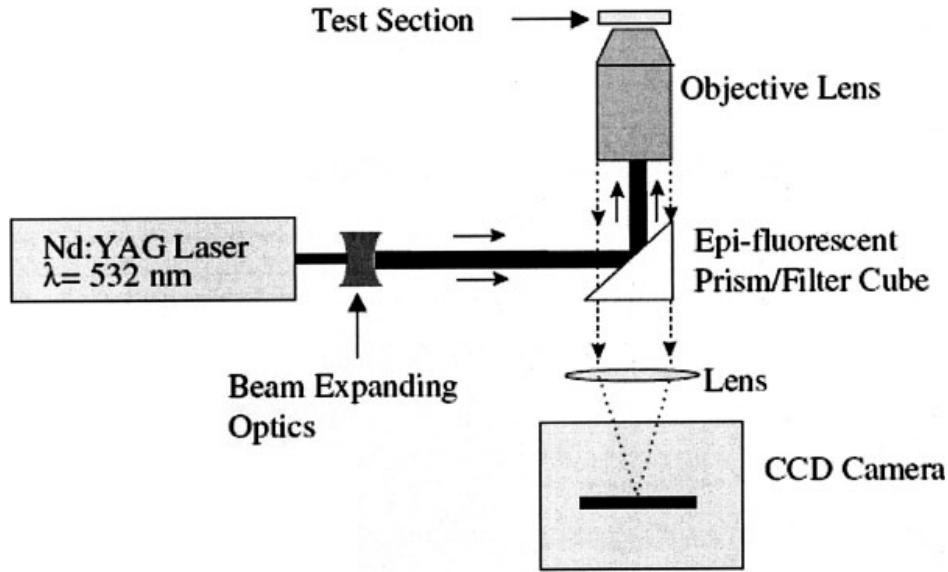


Figure 3. Principal setup of a microparticle image velocimetry (micro-PIV) system for acquisition inside a microfluidics device (from Meinhart et al.²⁰).

ent in the channel and the motion is driven by imposing a constant-pressure gradient. It is thus necessary to estimate the value of this pressure gradient according to experimental data. Therefore we calculate the pressure drop in the channel, assuming that the latter is filled with oil only. The pressure drop coefficient λ is given by

$$\lambda = \frac{\Delta P}{L} \frac{D}{\rho_c U_c^2} = \frac{64}{\text{Re}} \quad \text{with} \quad \text{Re} = \frac{\rho_c U_c D}{\mu_c} \quad 5$$

where L and D are the length of the periodic domain and the characteristic dimension of the channel section, respectively. Here $D = 60 \mu\text{m}$, so that the pressure gradient is $dP/dz = \Delta P/L = 6.58 \times 10^6 \text{ Pa/m}$.

Numerical constraints

Every explicit source term in the Navier–Stokes equations (that is, the capillary, inertial, and gravity terms, referred to as CAP, INE, and GRA, respectively) introduces a stability constraint on the numerical time step. In the present case, the time steps associated with the explicit contributions are $\Delta t_{\text{CAP}} = [(\rho_c + \rho_d)\Delta x^3/8\sigma]^{1/2} = 10^{-4}\tau$, $\Delta t_{\text{INE}} = \Delta x/U = 2 \times 10^{-2}\tau$, and $\Delta t_{\text{GRA}} = (\Delta x/g)^{1/2} = 7 \times 10^{-2}\tau$ (we take $\Delta x = 5 \times 10^{-3}D$ as the limiting grid size and $U = 0.05 \text{ m/s}$). The most restrictive constraint is clearly the one corresponding to capillary effects. Let us stress that its value is very small compared to “usual” time steps that are of $O(\tau)$. Therefore one needs a considerable number of time steps for the droplets to move significantly. This can lead to expensive computational time, particularly for 3D simulations (see the Results section below).

Micro PIV Inside Microdroplets

Microreactor setup

The microdevice we use is made of glass and PDMS (polydimethyl siloxane). The PDMS channels are cast onto a silica

wafer designed using SU8 resin soft lithography. They are stuck on a glass slide by contact after surface oxidation in a plasma chamber. As mentioned earlier, the channel section is rectangular. The two fluids are stored in syringes placed on syringe pumps (Model Ph2000; Harvard Apparatus, Holliston, MA) and are flushed at constant flow rates into polyethylene tubing connected to the microchannels. The dispersed phase is seeded with fluorescent microparticles. The aqueous droplets are naturally formed when the aqueous stream meets the oil stream at a T-junction. In our operating conditions, the selected regime for micro-PIV measurements corresponds to a droplet velocity of $4.5 \times 10^{-2} \text{ m/s}$. According to the expected forced velocity field inside the droplets, the range of values to be measured is estimated to lie between 0 and $9 \times 10^{-2} \text{ m/s}$.

Description of the micro-PIV system

To determine experimental velocity fields and profiles inside the droplets circulating in the microchannel, we used the LaVision (Cesson Sévigné, France) Imager Intense[®] charge-coupled device (CCD) camera/Axiovert 200 micro-PIV (Zeiss, Oberkochen, Germany) system, the principle of which is shown in Figure 3. The illumination beam is produced by two double-pulsed Nd:YAG (yttrium–aluminum–garnet) lasers. The laser beam is formed by a beam expander and directed to the objective lens of an inverted microscope (Axiovert 200M; Zeiss). The objective lens (Zeiss Epiplan Neofluar 20 \times) relays the light onto the microfluidic device, where it illuminates the entire flow volume. Fluorescent particles in the flow field absorb the green illumination light (532 nm) and emit a red light (612 nm). The emitted light passes through the fluorescent filter cube, where green light from background reflections is filtered out and the red fluorescent light from particles is recorded onto the CCD camera (LaVision Imager Intense[®], 12-bit double exposure, 10 Hz, 1376×1040 square pixels) and downloaded to a PC computer for processing. The principle of the signal processing is then rather similar to the one used in the

classical PIV technique and is described below. Velocity field calculation is achieved by use of Davis7 software.

Time and space resolution for the velocity field calculation

We choose to use an objective lens whose magnification is $M = 20\times$ and numerical aperture is $NA = 0.5$. It is immersed in air and offers a depth of field of 2.5 mm, which easily allows one to focus inside the channel passing through the 1-mm glass slide of the microdevice. Moreover, the magnification is well adapted to the droplet dimensions observed on the images: the observation window is $300 \times 400 \mu\text{m}^2$, which gives an image resolution of $0.29 \mu\text{m}/\text{pixel}$ according to the camera specification. By adapting the interrogation window size for the correlation calculation, a good description of the droplet dimensions and internal flow can be achieved.

The duration of one pulse of the laser is 5 ns. Within 500 ns after exposure, the image field is transferred to pixels storage onto the CCD camera, so that a second image field can be recorded by the CCD camera. After a specified time delay dt , a second laser pulse is used to record a second set of particle images onto the CCD camera. The window calculation size and the time delay dt have to be chosen so that the particles cross one fourth of the interrogation window on average between two pulses of the laser. We chose dt equal to $80 \mu\text{s}$, which gives a maximum displacement of the particles about 23 pixels between the two frames of an image pair. The instantaneous velocity field is eventually calculated by applying a cross-correlation between the two frames in a multipass mode, that is, using iterative calculations with several decreasing window sizes from 64×64 to 32×32 square pixels. Using an overlap of 50%, this provides about 300 velocity vectors inside a droplet horizontal plane (separated by intervals of $4.8 \mu\text{m}$).

The algorithm we use calculates the convolution product of the particles' intensities between the two frames of a couple of images for all the interrogation windows; a correlation maximum should emerge that corresponds to the most probable displacement of the particles. The interval between two couples of images depends on the lasers and camera frequencies. The lasers' frequency is 10 Hz. The camera frequency is limited by the downloading time to transfer the data from the pixels storage to the PC, which is 150 ms; the frequency of the camera is thus 15 Hz. Because the acquisitions are made in "double frame-double exposure" mode, the acquisition frequency of the couple of images is about 5 Hz. According to the velocity

of droplets, it is not possible to follow one droplet evolution along the channel. Using each couple of images, we first obtain an instantaneous velocity field; later we calculate the time-averaged velocity field using ≥ 40 droplets (the data are processed using Matlab[®] software, The MathWorks, Natick, MA). It is worth noting that no filtering nor "hole-filling" procedure is applied to the velocity field.

Characteristics of microparticles

The seeding particles that are added to the dispersed phase are polystyrene particles of diameter $d_p = 1 \mu\text{m}$. They come from Duke Scientific (R0100, Palo Alto, CA), are highly monodisperse (size uniformity $> 95\%$), and are uniformly spherical. The density ρ_p is 1050 kg/m^3 , which is comparable with the density of water; the refractive index is 1.59. We checked that these particles are good flow trackers. Indeed, in the Stokes flow regime, the relaxation time τ_p necessary for the particles to reach their terminal velocity can be calculated from

$$\tau_p = \frac{\rho_p d_p^2}{18\mu_d} \quad 6$$

Thus, $\tau_p = 0.058 \mu\text{s}$, which shows that the particles obviously reach their terminal velocity during the interval dt of $80 \mu\text{s}$ separating the two frames of an image pair. Besides, the falling velocity U_p is calculated from

$$U_p = \frac{1}{18} \frac{(\rho_p - \rho_d)g d_p^2}{\mu_d} \approx 0.03 \mu\text{m/s} \quad 7$$

which is clearly negligible compared with the measured velocities, which are of the order of 0.01 m/s. Because microparticles are used to trace the flow, one must consider errors arising from particle diffusion resulting from Brownian motion. A first-order error estimate relative to the displacement in the x -direction is given by Santiago et al.:²¹

$$\varepsilon_B = \frac{\langle s^2 \rangle^{1/2}}{\Delta x} = \frac{1}{U} \sqrt{\frac{2D_b}{dt}} \quad 8$$

where s^2 is the random mean-square particle displacement associated with the Brownian motion, U is the characteristic velocity, dt is the interval between two pulses, and D_b is the

Table 1. Comparison of Depths of Correlation*

This study	Experimental value	$9 \mu\text{m}$
LaVision reference	$\delta z = \frac{n_l \lambda}{2} \frac{n_l NA^2 + 342}{M \cdot NA}$	$10.5 \mu\text{m}$
Meinhart et al. ²²	$\delta z = \frac{3n_l \lambda}{NA^2} + \frac{2.16d_p}{\tan \theta} + d_p$	$7.4 \mu\text{m}$
Olsen and Adrian ²³	$\delta z = 2 \left[\frac{(1 - \sqrt{\varepsilon})}{\sqrt{\varepsilon}} \left(f^{\#2} d_p^2 + \frac{5.95(M+1)^2 \lambda^2 f^{\#4}}{M^2} \right) \right]^{1/2}$	$8.8 \mu\text{m}$

*Explanation of parameters: n_l , the refractive index of the fluid where the lens is immersed; λ , the wavelength of light emitted by the particles; NA , the numerical aperture of the objective; M , the total magnification of the system; d_p , the diameter of the seeding particles; ε , the value below which the particle does not contribute to the correlation function (10%); θ , the angle of collection of light ($\approx NA/D$); and $f^{\#}$, $f(n_l/NA) = 0.87$ (Bown et al.²⁴).

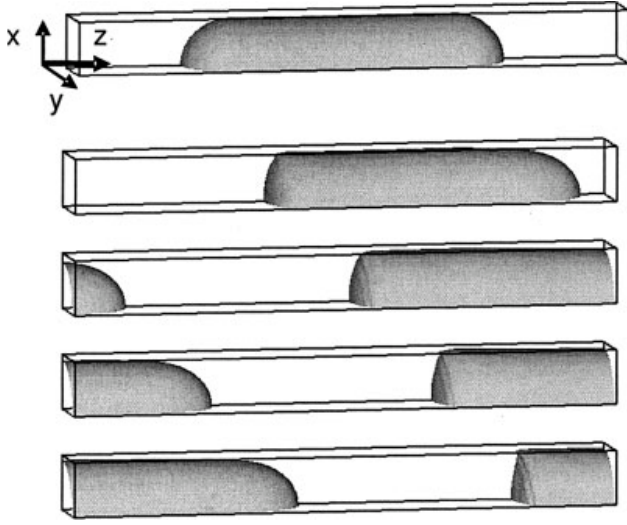


Figure 4. 3D computation of droplets in a microchannel.

Isosurface of volume fraction $C = 0.5$. The time interval between successive views is $\Delta\tau = \Delta t / (\rho_c D_{eq}^2 / \mu_c) = 1.81$.

Brownian diffusion coefficient, given by

$$D_b = \frac{kT}{3\pi\mu_d d_p} \quad 9$$

calculated at room temperature ($T = 298$ K) and where k is the Boltzmann constant. According to the operating conditions, ε_B is $< 1\%$, showing that the Brownian motion effects can be neglected.

Depth of correlation

In contrast to classical PIV, the illumination source is typically not a light sheet but rather an illumination of the whole flow volume. In this case, the measurement volume in micro-PIV is determined by the characteristics of the microscope lens (magnification and numerical aperture). The optical system focuses the particles that are within the depth of focus of the imaging system, whereas the remaining particles are unfocused and contribute to the background noise level. Thus, it is important to characterize exactly how thick the depth of correlation is. First, we measured it experimentally, as described in Meinhart et al.²² (see Appendix). According to our results, it can be concluded that the depth of correlation of the micro-PIV system is $9 \mu\text{m}$. This is in very good agreement with the theoretic

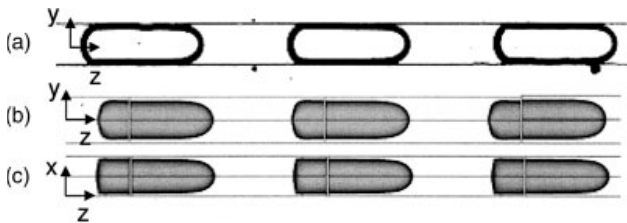


Figure 5. Shape of droplets.

(a) Experimental (yz) view imaged with a high-speed camera monitored on a microscope. (b) and (c) 3D computation.

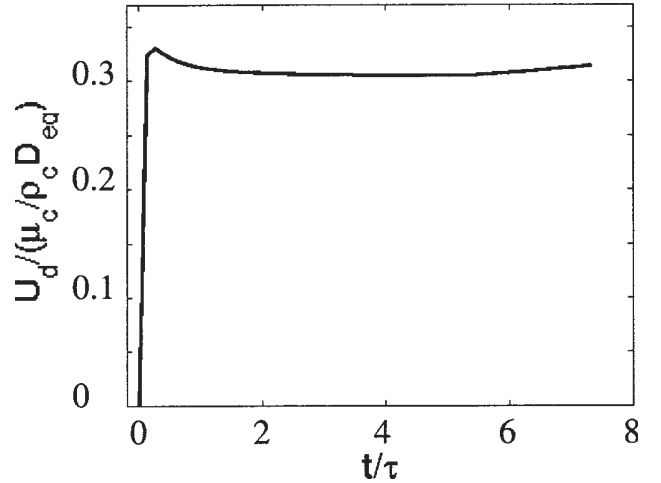


Figure 6. Computed droplet velocity (3D simulations).

cal values calculated in Table 1. Thus, according to the channel dimensions, one can describe the flow in at least five horizontal planes. By removing particles whose apparent diameter is $> d_p$, one can also increase the number of accessible measurements along the channel height. Hereafter we use $5\text{-}\mu\text{m}$ steps for the description of the flow along the channel height.

Results

Droplet shape

Figure 4 shows the computed droplet evolution. The numerical time step is $2.7 \times 10^{-5}\tau$; the final number of time steps is 275,000; the simulated physical time is about 7.3τ and the computational time is 49 days on a monoprocessor Intel[®] Pentium 4[®] CPU 3.00 GHz with 2 GB RAM. The droplet rapidly attains a bulletlike shape with a rounded head and a flat base. Figure 5 shows both the experimental and computed shape of the droplet train: the two series of results clearly exhibit a good qualitative agreement.

Velocity and flow rates

Figure 6 shows the computed velocity of the droplets. The flow is fully developed in a time of the order of the viscous time τ . Table 2 shows the comparison between computed and experimental velocity and flow rate. The computed flow rates are calculated as

$$Q_c = \frac{1}{L} \int_0^L \left[\int_S (I - C) U \cdot n dS \right] dz \quad \text{and} \quad Q_d = \frac{1}{L} \int_0^L \left[\int_S C U \cdot n dS \right] dz \quad (10)$$

Table 2. Comparison of the Computed and Measured Macroscopic Data

Parameter	Simulation	Experiments
Silicone oil velocity, U_c (m/s)	0.035	0.037
Silicone oil flow rate, Q_c (m^3/s)	7.2×10^{-11}	11×10^{-11}
Droplet velocity, U_d (m/s)	0.080	0.070 ± 0.025
Droplet flow rate, Q_d (m^3/s)	7.6×10^{-11}	2.8×10^{-11}

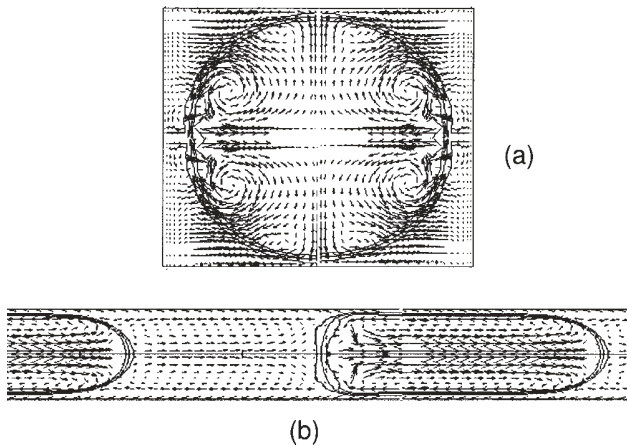


Figure 7. Velocity field in the reference frame of the droplet obtained inside the droplet and the continuous phase by 3D computations.

(a) View of the (xy) section at half of the droplet length. (b) View in the (yz) plane at $x/D = 0.4$. The interfacial region is represented by isovalues (C) of 0.05, 0.5, and 0.95.

where L and S are the length and the section of the channel, respectively; C is the volume fraction of the droplets; \mathbf{U} is the local velocity vector; \mathbf{n} is the unit vector normal to the surface element dS ; and z is the streamwise coordinate. The computed velocity is very close to the experimental values. The two flow rates are also of the same order of magnitude but it is difficult to obtain the same value through the two methodologies. Indeed, the computed value results from the imposed pressure drop, droplet volume, and frequency. The value of the pressure drop is estimated from continuous flow correlations (Eq. 5) but cannot a priori take into account the presence of droplets. As for the experimental velocity, the experimental device presents constraints that explain the velocity scatter such as (1) the porosity and swelling of the material, (2) the evolution of the wettability at the droplet generation, and (3) its extreme sensitivity to the pressure drop.

Velocity fields and forced convection inside the droplets

Figure 7 presents the computed velocity field in the reference frame of the droplet. Figure 7a shows the shape of a cross section of the droplet. The droplet shape is almost spherical, even though it is slightly flattened (the channel dimensions are $0.83D \times D$). We can notice that, because of capillary effects, the thickness of the liquid films separating the droplet from the top and bottom walls is half the thickness of the liquid films separating the droplet from the lateral walls (these thicknesses are $0.04D$ and $0.08D$ along the x - and y -axes, respectively). Note that these thicknesses would have been equal if the channel had a square cross section. In addition, capillary effects are responsible for the circulation of fluid across the section of the channel. Indeed, the interface of the droplet pushes the liquid away from the top and bottom walls, whereas it pulls it from the lateral walls. This effect might become significant as soon as either the channel aspect ratio, the confinement, or the surface tension becomes large.

Figure 7b reveals that in the central region of the droplet, the velocity is oriented toward the front, whereas in the vicinity of

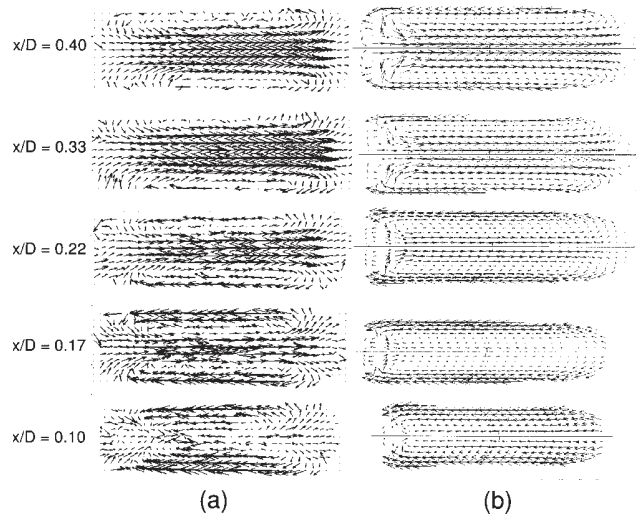


Figure 8. Velocity fields in the reference frame of the droplet in (yz) planes at different channel heights.

The height $x/D = 0.42$ corresponds to the horizontal symmetry plane; $x/D = 0$ corresponds to the location of the wall. (a) Micro-PIV experiments; (b) computed velocity fields (3D computation).

the lateral walls it is oriented towards the back of the droplet. Here the central region is much wider than the lateral one. The continuity of viscous stresses makes the liquid film of silicone oil (which is more viscous than water) drag the water located near the interface. Figure 8, which makes use of a reference frame attached to the droplet, compares the instantaneous computed velocity fields with the experimental ones. Five horizontal planes are shown; the first of them corresponds almost to the midplane of the channel, whereas the last one is located $6 \mu\text{m}$ down to the top wall. As expected, the central region where the flow is oriented toward the droplet head shrinks as the plane of visualization draws closer to the top wall. The computed velocity fields are in qualitative agreement with the experimental ones as shown in Figure 8.

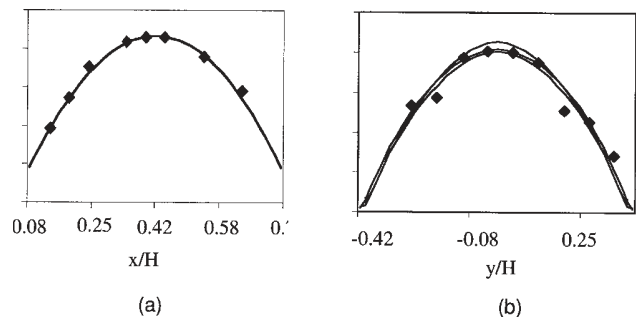


Figure 9. Transverse profiles of the longitudinal velocity (normalized by the averaged droplet velocity).

(a) In the vertical (xz) symmetry plane: (—) Computed velocity at half the droplet length; (◆) micro-PIV data at half the droplet length. (b) In the horizontal (yz) symmetry plane: (—) Computed velocity at $1/4$ – $1/2$ – $3/4$ of the total droplet length; (◆) micro-PIV data at half of the droplet length. Walls are located at normalized positions (a) $x/D = 0$ and $x/D = 0.83$, (b) $y/D = (-0.5)$ and $y/D = 0.5$.

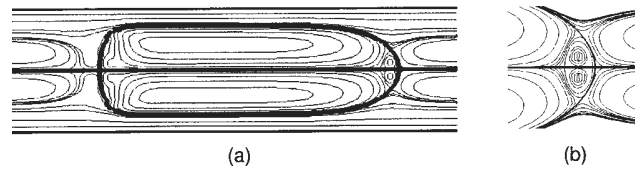
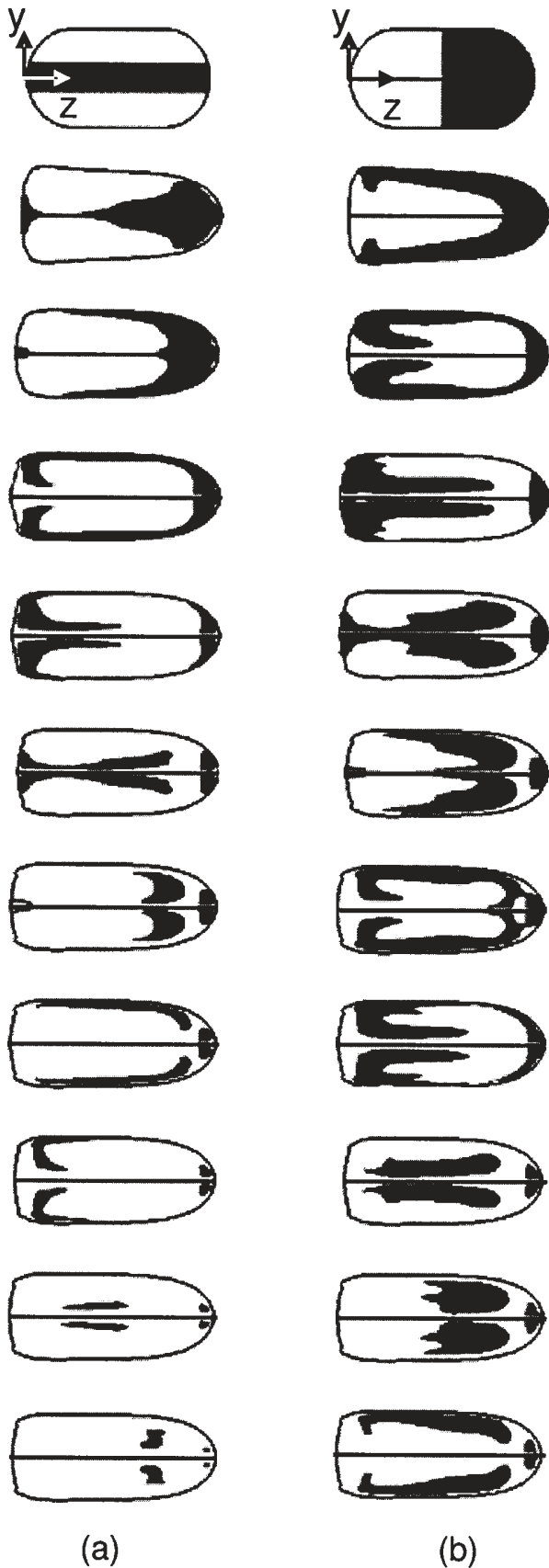


Figure 11. (a) Streamlines in the reference frame of the droplet obtained by 2D computations; (b) zoom on the droplet head.

Velocity profiles

Figure 9 compares the computed and measured longitudinal velocity profiles along the channel height and width, respectively. Figure 9b indicates that the velocity profile is almost independent of the longitudinal position in the droplet. Besides, the measured and computed profiles are in good agreement.

Mixing

Here dye is “numerically” injected into the droplets. The aim is to reproduce the mixing caused by advection inside the droplet and so to detect regions where mixing is not efficient. Numerically speaking, a new color function is defined that equals 1 in cells filled by dye and equals 0 elsewhere. This color function is transported by solving Eq. 2. We assume that (1) dye has no effect on the flow and (2) molecular diffusion is negligible compared to convective mixing. As a consequence, the slight diffusion that might be observed is purely the result of numerical diffusion. The first views of Figures 10a and 10b show the two initial configurations that were selected. By taking advantage of symmetry along the z -axis, only half of the droplet is simulated. The computations in this section are performed within a 2D (yz) domain $0.5D \times 5D$ large. The flow is initially at rest; the initial height and length of the droplet are $0.83D$ and $2D$, respectively. A free-slip (resp. no-slip) condition is imposed on the bottom (resp. top) boundary; the lateral boundaries are periodic. The grid size is 30×180 and is refined near the walls as already described for the 3D case.

Figure 10 shows mixing of the dye for the two selected cases. These cases correspond to two different situations experimentally encountered because of the method of reactant injection (flow focusing or interdrop coalescence). The numerical time step is $3.3 \times 10^{-5}\tau$; the final number of time steps is 400,000; the simulated physical time is 13.4τ and the computational time is 20 h. Both cases exhibit the formation of two counterrotating recirculation zones separated by the symmetry axis. There are clearly some regions inside the droplet where

Figure 10. 2D simulations showing dye mixing inside droplets, where (a) dye is injected along the horizontal symmetry plane or (b) dye is injected throughout the front half of the droplet.

The time interval between successive views is $\Delta\tau = \Delta t / (\rho_h D_{eq}^2 / \mu_h) = 1.97$. The horizontal black line is the symmetry axis. Dye concentration ranges from 0 to 1. The drop interface is represented by the isoline $C = 0.5$. The black zone corresponds to a concentration of the dye > 0.55 .

no mixing occurs, especially at the head and at the back of the droplet. This is in agreement with experimental observations (see Figure 1b). These regions are made clearer in Figure 11, which displays the streamlines of the flow in the reference frame of the droplet. Figure 11b is a zoom on the head of the droplet: the recirculation zone in the droplet head is clearly revealed. This zone is not visible at the back of the droplet because there is some numerical spreading of the interface in this region that smoothes the velocity field. Nevertheless, Figure 11 clearly shows that this recirculation zone exists.

Conclusion

The dynamics of a droplet in a rectangular microchannel is followed using a direct numerical approach. The 3D computations show a good agreement with micro-PIV measurements and the shape of the deformed droplet is well reproduced. The complete 3D dynamics of the liquid–liquid flow are obtained in a rectangular-section channel. This gives access to the flow structures generated inside the droplets, which can influence the transfer with the continuous phase. Besides, 2D computations are performed and a tracer is numerically injected inside the droplet, starting with two different initial conditions. The results reveal the presence of internal zones at the front and back of the droplets where mixing remains mainly arising from diffusion. This work should be extended in several ways (1) by changing proportionally the dimensions of the channel and the droplet so as to study scaling effects, (2) by changing the ratio between the channel and the droplet size to evaluate the importance of the confinement on the mixing, and (3) by investigating the influence of dimensionless parameters such as the Capillary number or the Reynolds number on the mixing efficiency.

Acknowledgments

This work was financially supported by a Rhodia grant and the Institut National Polytechnique de Toulouse (INPT).

Literature Cited

1. Song H, Tice JD, Ismagilov R. A microfluidics system for controlling reaction networks in time. *Angew Chem Int Ed Engl.* 2003;42:768–771.
2. Sarrazin F, Prat L, Casamatta G, Gourdon C, Joanicot M. Mixing characterisation in micro-drops. Proceedings of the 7th World Congress of Chemical Engineering, Glasgow, UK, July, 2005.
3. Sarrazin F, Prat L, Gourdon C, Casamatta G, Joanicot M. Mixing characterization and fast reactions in micro-drops. Sustainable (bio)chemical process technology. Proceedings of the 6th International Conference on Process Intensification for the Chemical Industry, Delft, The Netherlands, September, 2005.
4. Holdych DJ, Georgiadis JG, Buckius RO. Hydrodynamic instabilities of near-critical CO₂ flow in microchannels: Lattice–Boltzmann simulation. *Phys Fluids.* 2004;16:1791–1802.
5. Ghidersa BE, Wörner M, Cacuci DG. Exploring the flow of immiscible fluids in a square vertical mini-channel by direct numerical simulation. *Chem Eng J.* 2004;101:285–294.
6. Harries N, Burns JR, Barrow DA. A numerical model for segmented flow in a microreactor. *Int J Heat Mass Transfer.* 2003;46:3313–3322.
7. Kashid MN, Gerlach I, Goetz S. Internal circulation within the liquid slugs of a liquid–liquid slug-flow capillary microreactor. *Ind End Chem Res.* 2005;44:5003–5010.
8. Coulliette C, Pozrikidis C. Motion of an array of drops through a cylindrical tube. *J Fluid Mech.* 1998;358:1–28.

9. Muradoglu M, Stone HA. Mixing in a drop moving through a serpentine channel: A computational study. *Phys Fluids.* 2005;17:073305.
10. Cristobal G, Arbouet L, Sarrazin F, Talaga D, Bruneel JL, Joanicot M, Servant L. On-line laser Raman spectroscopic probing of droplets engineered in microfluidic devices. *Lab Chip.* 2006;B602702D.
11. Dummann G, Quittmann U, Gröschel L, Agar DW, Wörz O, Morgenweiss K. The capillary-microreactor: A new reactor concept for the intensification of heat and mass transfer in liquid–liquid reactions. *Catal Today.* 2003;79–80:433–439.
12. Burns JR, Ramshaw C. The intensification of rapid reactions in multiphase systems using slug flow in capillaries. *Lab Chip.* 2001;1:10–15.
13. Brackbill JU, Kothe DB, Zemach C. A continuum method for modeling surface tension. *J Comput Phys.* 1992;100:335–354.
14. Magnaudet J, Rivero M, Fabre J. Accelerated flows around a rigid sphere or a spherical bubble. Part I: Steady straining flow. *J Fluid Mech.* 1995;284:97–135.
15. Calmet I, Magnaudet J. Large eddy simulation of high-Schmidt-number mass transfer in a turbulent channel flow. *Phys Fluids.* 1997;9:438–455.
16. Legendre D, Magnaudet J. The lift force on a spherical bubble in a viscous linear shear flow. *J Fluid Mech.* 1998;368:81–126.
17. Zalesak ST. Fully multidimensional flux-corrected transport algorithms for fluids. *J Comput Phys.* 1979;31:335–362.
18. Bonometti T, Magnaudet J. An interface capturing method for incompressible two-phase flows. Validation and application to bubble dynamics. *Int J Multiphase Flow.* doi:10.1016/j.ijmultiphaseflow.2006.07.003.
19. Bonometti T, Magnaudet J. Transition from spherical cap to toroidal bubbles. *Phys Fluids.* 2006;18:052102.
20. Meinhardt CD, Wereley ST, Santiago JG. PIV measurements of a microchannel flow. *Exp Fluids.* 1999;27:414–419.
21. Santiago JG, Wereley ST, Meinhardt CD, Beebe DJ, Adrian RJ. A particle image velocimetry system for microfluidics. *Exp Fluids.* 1998;25:316–319.
22. Meinhardt CD, Wereley ST, Gray MHB. Volume illumination for two-dimensional particle image velocimetry. *Meas Sci Technol.* 2000;11:809–814.
23. Olsen MG, Adrian RJ. Brownian motion and correlation in particle image velocimetry. *Optics Laser Technol.* 2000;32:621–627.
24. Bown MR, MacInnes JM, Allen RWK. Micro-PIV simulation and measurement in complex microchannel geometries. *Meas Sci Technol.* 2005;16:619–626.

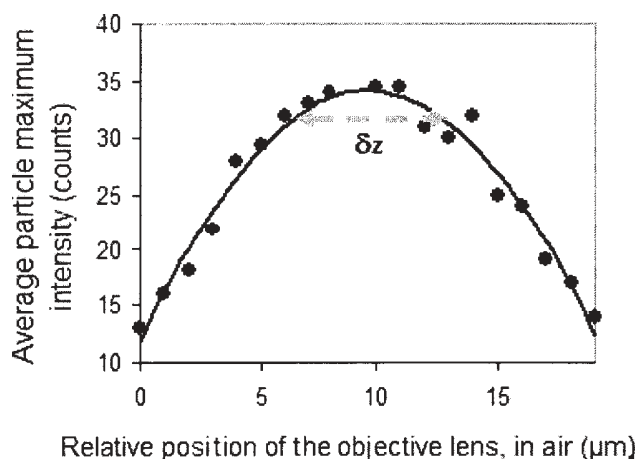


Figure A1. Average particle maximum intensity vs. the distance from the focus plan.

The distance should be calculated by taking into account the ratio between the refractive index of the water (in which the particles are immersed) and the refractive index of the air (in which the lens is immersed): $n_{\text{water}}/n_{\text{air}} = 1.3$, which gives a corrected δz of 9 μm .

Appendix: Experimental Determination of the Depth of Correlation

The method we use is described in Meinhart et al.²² A droplet of the seeding microparticle suspension is inserted between two microscope glass slides. Several images are taken at $1\text{-}\mu\text{m}$ steps of the objective lens. For each vertical position along the x -axis, the mean maximal intensity of the particles $\langle I_x \rangle$ is determined, as

shown in Figure A1. According to analytical estimates, the particles do not contribute to the correlation function if their maximum intensity is $<90\%$ of the in-focus image maximum intensity. Consequently, the depth of correlation is twice the distance from the focus plan over which $\langle I_x \rangle$ is 10% around the maximum value.

Manuscript received Mar. 24, 2006, and revision received Aug. 25, 2006.
